



# Stratospheric Extinction Profiles from SCIAMACHY Solar Occultation

Stefan Noël, Klaus Bramstedt, Alexei Rozanov, Elizaveta Malinina, Heinrich Bovensmann, and John P. Burrows

Institute of Environmental Physics, University of Bremen, FB 1, P.O. Box 330440, 28334 Bremen, Germany

**Correspondence:** S. Noël (stefan.noel@iup.physik.uni-bremen.de)

## Abstract.

The SCIAMACHY (Scanning Imaging Absorption Spectrometer for Atmospheric CHartographY) instrument on ENVISAT provided between August 2002 and April 2012 measurements of solar and Earthshine spectra from the UV to the SWIR spectral region in multiple viewing geometries.

5 We present a new approach to derive stratospheric aerosol extinction profiles from SCIAMACHY solar occultation measurements based on an onion peeling method similar to the Onion Peeling DOAS (Differential Optical Absorption Spectroscopy) retrieval, which has already been successfully used for the derivation of greenhouse gas profiles. Since the retrieval of aerosol extinction requires as input measured transmissions in absolute units, an improved radiometric calibration of the SCIAMACHY solar occultation measurements has been developed, which considers various instrumental and atmospheric effects specific to  
10 solar occultation.

The extinction retrieval can in principle be applied to all wavelengths measured by SCIAMACHY. As a first application, we show results for 452 nm, 525 nm and 750 nm. The whole SCIAMACHY solar occultation time series has been processed, covering a latitudinal range of about 50–70°N. Reasonable extinctions are derived between about 15 and 30 km with typically larger uncertainties at higher altitudes due to decreasing extinction.

15 Comparisons with collocated SAGE II and SCIAMACHY limb aerosol data products revealed a good agreement with essentially no mean bias. However, depending on altitude differences of up to  $\pm 20$ –30% to SAGE II at 452 nm and 525 nm are observed. These differences are mainly caused by systematic vertical oscillations in the SCIAMACHY occultation data. The agreement with SCIAMACHY limb data is even better (typically within 5–10% between 17 and 27 km).

20 Major volcanic eruptions as well as occurrences of PSCs can be identified in the time series of extinction data and related anomalies. Influence of the Quasi-Biennial-Oscillation (QBO) are visible above 25 km. Estimated linear changes of extinction between 2003 and 2011 reach 20–30% per year at 15 km, mainly because all relevant volcanic eruptions (above 50°N) occurred after 2006.



## 1 Introduction

Stratospheric aerosols play an important role in climate as they affect radiative forcing either by scattering and absorption of light (direct effect) or by their impact on clouds (indirect effect). In addition, aerosols affect the creation of polar stratospheric clouds (PSCs) on which surfaces  $O_3$  depletion takes place.

The main constituents of stratospheric aerosols are sulfuric acid ( $H_2SO_4$ ) and (liquid) water ( $H_2O$ ). Sulfuric acid is mostly produced from oxidation of carbonyl sulfide (OCS) and sulfur dioxide ( $SO_2$ ). OCS has mostly marine origin while  $SO_2$  mainly originates from volcanic eruptions, biomass burning (both natural and anthropogenic origin) and fossil fuel combustion. The main transport path of OCS and  $SO_2$  in the stratosphere during volcanic quiescent periods is the tropical upwelling. In addition, anthropogenic  $SO_2$  from fossil fuel combustion is transported to the stratosphere via the Asian monsoon (Randel et al., 2010) while pyrocumulus events represent a transport mechanism for biomass burning products. Large amounts of  $SO_2$  can be directly injected into the stratosphere by strong volcanic eruptions.

Information about stratospheric aerosols can be derived e.g. from ground based lidars or in-situ balloon and aircraft measurements. However, these usually have a limited spatial and temporal coverage. Global measurements of stratospheric aerosols are only possible with satellite based instruments, see Table 1.

These started in the 1970ies with the suite of SAM (Stratospheric Aerosol Measurement) and SAGE (Stratospheric Aerosol and Gas Experiment) instruments (see e.g. Chu and McCormick, 1979; Kent and McCormick, 1984; McCormick, 1987; Osborn et al., 1989; Russell and McCormick, 1989; Thomason and Taha, 2003; Thomason et al., 2008).

From 1991 until 2001 HALOE (Halogen Occultation Experiment on the Upper Atmosphere Research Satellite (UARS); see e.g. Russell et al., 1993; Lee et al., 2001) performed occultation measurements from which among other atmospheric constituents also aerosol extinctions were derived. Aerosol extinction profiles were also provided by the Polar Ozone and Aerosol Measurement (POAM) II and III between 1993 and 2005 (see e.g. Bevilacqua et al., 1995; Randall et al., 1996). These were accompanied between 2002 and 2012 by the ENVISAT instruments GOMOS (Global Ozone Monitoring by Occultation of Stars; Kyrölä et al., 2010), MIPAS (Michelson Interferometer for Passive Atmospheric Sounding; Fischer et al., 2008) and SCIAMACHY (Scanning Imaging Absorption Spectrometer for Atmospheric CHartography; see e.g. Gottwald and Bovensmann, 2011). Currently, OSIRIS (Optical Spectrograph and InfraRed Imager System, see e.g. Llewellyn et al., 2004; Bourassa et al., 2012; Rieger et al., 2014, 2019), CALIOP (Cloud-Aerosol Lidar with Orthogonal Polarization Lidar; Winker et al., 2007; Vernier et al., 2011), OMPS (Ozone Mapping Profiler Suite; Jaross et al., 2014; Loughman et al., 2018; Chen et al., 2018), and SAGE III (from ISS; Cisewski et al., 2014) are still operational and deliver data on stratospheric aerosols.

These satellite instruments measure via different viewing geometries, all having advantages and drawbacks. Occultation instruments can more or less directly measure aerosol extinction (i.e. the sum of scattering and absorption of light), whereas limb sounders are typically more sensitive to smaller particles (Malinina et al., 2019). Limb data are usually more difficult to be analysed, see e.g. Malinina et al. (2018), who derived particle size distributions from SCIAMACHY limb measurements.

In the following we describe a new method to derive stratospheric aerosol extinction profiles from SCIAMACHY solar occultation data. This method is in principle able to derive extinction profiles at any wavelength measured by SCIAMACHY.



To demonstrate this, we concentrate in the current study on selected wavelengths in the visible / near infrared spectral region where also suitable correlative data sets (SAGE II and SCIAMACHY limb) are available, namely 452 nm, 525 nm and 750 nm.

The manuscript is organised as follows: Section 2 lists the input data used in this study. In Section 3 the SCIAMACHY occultation data are described with the focus on the newly developed radiometric calibration, which is the largest challenge in this context. Section 4 explains the extinction retrieval method. The corresponding retrieval results and their first validation are then shown in Section 5. In Section 6 we show time series of the extinction data and derive from these estimates for linear changes within the time interval of the SCIAMACHY measurements. The conclusions are summarised in Section 7. Some details on the methods used in this study are given in the appendix.

## 65 2 Used data

### 2.1 SCIAMACHY spectra

The SCIAMACHY solar occultation data used in this study were extracted from the SCIAMACHY Level 1 Version 8 product with all calibrations applied except for polarisation correction as solar irradiances are unpolarised. Additional pointing corrections as described in Bramstedt et al. (2017) have been applied such that the tangent height knowledge is better than 26 m. These radiance measurements are then converted into transmissions using additional corrections as will be described in detail in section 3.

### 2.2 ECMWF ERA Interim

ECMWF ERA Interim model data (Dee et al., 2011) are used in the retrieval to account for actual pressure and temperature profiles (see section 4.1). These data are available every 6 hours on a  $0.75^\circ$  horizontal grid and on 60 altitude levels.

### 75 2.3 SAGE II profiles

The SAGE II instrument performed solar occultation measurements from 1984 to 2005 and provided extinction profiles at several wavelengths (386 nm, 452 nm, 525 nm, 1020 nm) as well as profiles of  $O_3$ ,  $NO_2$  and  $H_2O$ . In this study we use SAGE II V7.00A sunset extinction data (Damadeo et al., 2013) from the overlap period with SCIAMACHY (2002 to 2005) at 452 nm and 525 nm for comparisons. We selected collocated data within a maximum spatial distance of 800 km and a maximum temporal distance of 9 h. However, the latter is no major restriction; since both data sets are based on sunset measurements, the actual temporal differences are always smaller than 1 h.

### 2.4 SCIAMACHY limb aerosol

The SCIAMACHY limb aerosol extinction product V1.4 was obtained by using the algorithm described in Rieger et al. (2018). It comprises stratospheric profiles derived from SCIAMACHY limb measurements at 750 nm. The data have been filtered according to the recommendations given by the data providers in the accompanying README file; especially, invalid data



and data points with a vertical resolution larger than 7 km or extinctions exceeding  $0.1 \text{ km}^{-1}$  have not been used. The spatial collocation criterion is the same as for SAGE II, but we used a maximum temporal distance of 10 h. This is necessary to achieve also collocations in summer.

### 3 SCIAMACHY occultation

#### 90 3.1 Measurements

The SCIAMACHY instrument performed measurements in nadir, limb and solar/lunar occultation geometry covering continuously the spectral range from about 214 nm to 1750 nm and two additional bands at around 2000 nm and 2400 nm.

SCIAMACHY performed solar occultation measurements every orbit in the Northern hemisphere (between about  $50^\circ\text{N}$  to  $70^\circ\text{N}$ ) during time of (local) sunset. During such a measurement SCIAMACHY observed the (apparently) rising sun through  
95 the atmosphere with the following typical measurement sequence (see also Fig. 1, from Noël et al., 2016):

1. Perform a sequence of up- and downward scans around an altitude of 17.2 km until the centre of the (un-refracted) sun reaches this altitude.
2. Switch-on the so-called sun follower in azimuthal direction to horizontally align the viewing direction to the intensity centre of the sun.
- 100 3. Follow the rising sun while scanning vertically around the (predicted) centre of the sun until about a tangent altitude of 100 km.

Above 100 km either special solar calibration measurements are performed or the scan over the sun is continued up to about 250 km. In this study, we concentrate on data below 100 km, such that all available solar occultation measurements can be used.

#### 105 3.2 Transmissions

The extinction retrieval (see below) requires as input atmospheric transmissions. In order to derive these transmissions, the individual SCIAMACHY spectra are in a first step normalised to a reference spectrum obtained at a high tangent altitude of about 90 km.

This is done independently for up- and downward scans. With this, all possibly erroneous multiplicative calibration factors  
110 (e.g. most degradation effects or systematic errors in radiometric calibration) cancel out, which is why occultation measurements are sometimes called ‘self-calibrating’.

However, this is not really the case for SCIAMACHY because of the scan over the sun. The width of the instantaneous field of view (IFOV) of SCIAMACHY is in solar occultation mode about  $0.7^\circ$ , the height about  $0.045^\circ$ . As the diameter of the sun is about  $0.5^\circ$ , this implies a strongly varying signal over the scan as different parts of sun are seen at each readout. Furthermore,



115 refraction effects and additional problems due to e.g. mispointing and jumps in the signal when switching on the sun follower  
need to be taken into account. This is explained in the following subsections.

### 3.2.1 Radiometric calibration / scan correction

The largest impact on the measured signal is related to the area of the sun seen during each readout, which varies over the scan.  
This is mainly a geometric effect, which is illustrated in Fig. 2. Depending on the vertical position of the SCIAMACHY IFOV  
120 relative to the centre of the sun different areas of the IFOV are illuminated. The measured signal then varies approximately  
with the size of the illuminated area.

The right plots of Fig. 3 show exemplary for 525 nm this varying signal for the reference scan at high tangent altitudes, where  
atmospheric absorption and refraction are small and can be neglected. All data are normalised to the (interpolated) maximum  
signal of the scan. In the top right figure the signal is shown for an upward and a downward scan as function of geometric  
125 tangent altitude. Because the sun is (relative to the instrument) rising during the measurement, an upward scan covers a larger  
altitude range than a downward scan. However, as can be seen in the bottom right figure, the variation of the signal becomes  
very similar when plotted as function of angular (vertical) distance from the centre of the sun. The thick black line in this figure  
shows the result of a simple geometrical model of the varying area when assuming a circular sun disk of diameter  $0.26^\circ$  with  
homogeneous brightness. The overall shape of the measurements is reproduced quite well by the black line; the deviations  
130 are caused by the facts that 1) the real sun does not have the same brightness everywhere (mainly because of limb darkening  
effects) and 2) the measured signal is an integral over the IFOV in vertical direction ( $0.045^\circ$  correspond to about 2.6 km) which  
smears out the black curve along the x axis.

The left plots of Fig. 3 show the corresponding measured transmissions for various scans at lower tangent altitudes as  
function of tangent height (top left) and distance to the sun centre (bottom left). The normalisation is the same as for the  
135 right plots, i.e. all upward/downward scans (even/odd numbers) are normalised to the maximum value of of the reference  
measurement (green/red curve in the right plot). Due to increased atmospheric absorption and scattering the transmissions  
decrease at lower altitudes. In addition, as can be seen in the bottom left plot, the maximum signal of the scan shifts to the right  
with decreasing altitude due to increasing refraction.

The plots of Fig. 3 also show that the measured signal for one scan is not symmetrical relative to the sun centre, i.e. the  
140 signal drops to zero only on one side. This is because the position and elevation rate of the sun assumed in the commanding  
of the measurement was derived from predicted orbital information. This results in a scan which is not exactly centred on the  
(true) sun. This may also lead to azimuthal offsets (see right plot of Fig. 2), which are corrected by use of the sun follower (see  
above), but this can introduce jumps in the signal at altitudes around 17 km which require special treatment (see Appendix A).

To correct for the scan effect, we define a (numerical) sun shape function  $S$ , which is the interpolated measured transmission  
145 ( $T^m$ ) for a scan around a reference altitude of about 90 km as function of angular distance from the centre of the sun ( $\alpha$ ), as  
shown in Fig. 3 (bottom right). This is done for each measurement and independently for both up- and downscan in order to  
reduce possible systematic effects caused by the scan direction.



The actual  $\alpha$  is then calculated for each measurement by using the viewing direction (defined by the line-of-sight (LOS) zenith angle  $\gamma$ ) and the direction of the ‘true’ sun (i.e. without refraction)  $\beta$ . The latter is essentially the solar zenith angle (SZA) at the satellite, i.e.  $\beta = 180^\circ - \text{SZA}$ . The LOS zenith angle  $\gamma$  and the solar zenith angle are given in the SCIAMACHY Level 1 product for the centre of the IFOV. As we assume a horizontally homogeneous atmosphere (within the range of one measured profile) azimuthal differences are not relevant in this context. However, as mentioned before, possible azimuthal jumps at lower altitudes need to be considered, see Appendix A.

To account for refraction effects we use a simple model similar to the one used in the SAGE II project (Damadeo et al., 2013), see Fig. 4. It is assumed that refraction occurs only at the tangent point with the basic parameter being the bending angle ( $\delta$ ). This bending angle decreases with altitude and is essentially a function of pressure. In the stratosphere, the overall altitude variation of  $\delta$  can therefore be described by an exponential function of tangent height  $z$ :

$$\delta = \exp(a + b z) \quad (1)$$

The parameters  $a$  and  $b$  depend on atmospheric conditions (and also on wavelength) and are different for each measured profile.  $b$  is typically negative, as refraction effects decrease with altitude. Therefore we determine these parameters from the measurements (see Appendix B). From these we then get for each measurement the bending angle  $\delta$  from which we calculate the distance  $\alpha$  of the observed point on the sun to the sun centre via:

$$\alpha = \gamma - \beta - \delta \quad (2)$$

The expected transmission corresponding to this distance is then given by the sun shape function  $S(\alpha)$  derived from the reference scans (see above). The scan-corrected transmission  $T$  as function of tangent altitude  $z_i$  for readout  $i$  of an occultation measurement is then given by:

$$T_i = T(z_i) = T_i^m / S(\gamma_i - \beta_i - \delta_i) \quad (3)$$

### 3.3 Selection of subset of readouts

Prior to the retrieval (see Section 4.1) the measured transmissions need to be interpolated to a fixed altitude grid. Therefore it is sufficient to use only a subset of the measured spectra for this. This subset is basically selected by using readouts with the highest (uncorrected) transmission signal, which corresponds e.g. to the envelope of the data points shown in the top left plot of Fig. 3. As an additional criterion, we only take data points with an altitude difference of 0.5 km or larger (when starting at the top and then going downwards in altitude). An example showing the results of this procedure is given in section 5.1.

## 4 Retrieval method

The basic idea for the aerosol extinction retrieval is to use a two step approach:

1. Apply the Onion Peeling DOAS (Differential Optical Absorption Spectroscopy) retrieval method to correct the measured transmissions for Rayleigh scattering and gas absorptions.



2. Use an onion peeling method to determine extinctions from corrected transmissions for different altitude layers, starting with the highest layer.

180 These two steps are described in more detail in the following sub-sections.

With this approach it is possible to determine extinctions even at wavelengths where gases absorb (since this absorption is fitted). In addition, the method also delivers profiles of the absorbing gases. However, these derived stratospheric gas profiles (in the present case for O<sub>3</sub> and NO<sub>2</sub>) are not the primary focus of the current study as retrieval settings are optimised for aerosol extinction.

## 185 4.1 Onion Peeling DOAS Approach

The Onion Peeling DOAS (ONPD) retrieval method has been originally developed to derive stratospheric profiles of greenhouse gases. So far, it has been applied to the retrieval of water vapour, CO<sub>2</sub> and methane (Noël et al., 2010, 2011, 2016, 2018). The retrieval method is described in detail in these publications; we therefore give here only a basic summary and the specific settings used in the context of this study.

### 190 4.1.1 Description of method

In the ONPD approach the atmosphere is divided into layers. All measured transmission spectra are interpolated to this grid. For each tangent height  $j$  a weighting function DOAS fit (see e.g. Coldewey-Egbers et al., 2005) is performed using the following formula:

$$\ln T_j^{\text{interp}} = \ln T_{j,\text{ref}} + \sum_k \sum_i w_{ij,k} a_{i,k} + P_j \quad (4)$$

195 Here,  $T_j^{\text{interp}}$  is the (interpolated) measured transmission for tangent height  $j$ .  $T_{j,\text{ref}}$  is a reference transmission derived for the same viewing geometry from a radiative transfer model, in our case SCIATRAN V3.7 (Rozanov et al., 2013) in occultation mode. The index  $i$  refers to the atmospheric layers,  $k$  to the different absorbers considered in the fit.  $w_{ij,k}$  is the relative weighting function, which is also derived by the radiative transfer model. It describes how the (logarithmic) transmission for tangent height  $j$  changes if the amount of absorber  $k$  is changed by 100% in layer  $i$ .  $a_{i,k}$  is a scalar factor, which describes  
200 the actual change of absorber  $k$  in layer  $i$  relative to the assumptions in the radiative transfer model. Spectrally broadband absorption and scattering (especially due to aerosols) is described by a polynomial  $P_j$ .

The factors  $a_{i,k}$  and the polynomial  $P_j$  are fitted for each layer  $j$ , starting at the top layer and then propagating downwards. In each step the results of the upper layers are taken into account. From the combination of the  $a_{i,k}$  scaling factors with the a-priori profiles assumed in the radiative transfer calculations vertical profiles of the absorbers  $k$  are derived. These profiles are then  
205 vertically smoothed using a boxcar of width 4.3 km to account for the vertical resolution of the measurements and to reduce vertical oscillations. This smoothing essentially also defines the vertical resolution of the resulting profiles. Reasonable results for greenhouse gases are achieved for altitudes between about 17 and 45 km, see e.g. Noël et al. (2018). At the wavelengths





considered in the present study and with the improved calibration performed here we expect that this validity range can be extended even to somewhat lower altitudes, see also below.

#### 210 4.1.2 Specific settings and sequence of fits

The general ONPD settings are the same as described in Noël et al. (2018). We use a vertical layering from 0 to 50 km with 1 km steps. In general, the ONPD method uses a fixed data base of reference transmissions derived with SCIATRAN assuming conditions of the 1976 US standard atmosphere (NASA, 1976). We correct for the actual conditions by using corresponding weighting functions via Eq. (4). For pressure and temperature this is done by using as input data from the ECMWF ERA  
215 Interim model. We select the profiles spatially and temporally closest to the measurements and interpolate them to the ONPD altitude grid.

In the current study, we have performed calculations for three different extinction wavelengths  $\lambda_{\text{ext}}$  (452, 525 and 750 nm). The degree of the fitted polynomial is 2 in these cases. For consistency reasons and because the fitting windows are optimised for the extinction retrieval we use a specific sequence of retrievals such that information obtained in one retrieval can be used  
220 in other retrievals. Therefore we start with the retrieval for  $\lambda_{\text{ext}}=525$  nm, from which we obtain  $\text{O}_3$  and  $\text{NO}_2$  profiles which are then used in the other retrievals. The detailed settings for each retrieval are summarised in Table 2.

#### 4.2 Extinction retrieval

The standard ONPD method does not require fully calibrated data as input as the fitted polynomials  $P_j$  also account for possible multiplicative radiometric offsets, i.e. as caused by the scan over the sun.

225 In the present study we use fully calibrated transmissions as input. Therefore, the polynomials  $P_j$  should essentially contain information about extinction in the atmosphere. This can be described by the following formula:

$$P_j(\lambda_{\text{ext}}) = - \sum_i \epsilon_i(\lambda_{\text{aer}}) l_{ij}(\lambda_{\text{aer}}) \quad (5)$$

$P_j(\lambda_{\text{ext}})$  is the value of the polynomial  $P_j$  derived from the ONPD retrieval at the wavelength  $\lambda_{\text{ext}}$ , at which we want to determine the extinction.  $l_{ij}$  is a (fixed) geometric factor which describes the length of the occultation light path in layer  $i$  when  
230 looking layer  $j$ . These path lengths are also derived from SCIATRAN for each atmospheric layer and viewing direction and consider refraction. They therefore also depend slightly on wavelength.  $\epsilon_i$  is the extinction in layer  $i$ ; this is the quantity we want to derive.

This is done – consistently with the ONPD approach – by use of an onion peeling method: We start at the top layer and then propagate downwards while taking into account the results from above. Contributions from below the current tangent  $j$  (due to  
235 refraction and vertical size of the IFOV) are considered by assuming  $\epsilon_i = \epsilon_j$  for  $i < j$  when determining  $\epsilon_j$ . Since extinction typically increases with decreasing altitude this results in a small over-estimation, but gives a stable solution.





## 5 Results

### 5.1 Example 11 September 2003

To illustrate the outcome of the different calibration and retrieval parts described in the previous section we present in this subsection as an example the results for orbit 8014 (on 11 September 2003). This orbit has been selected due to a close collocation of a corresponding SAGE II measurement, such that a direct comparison of extinction results is possible (see below).

Fig. 5 shows the transmissions as function of altitude for the three selected extinction wavelengths. In the left column the uncorrected transmissions (i.e. without scan correction) are shown in red (similar to the data shown in the top left graph of Fig. 3). The black dots denote the selected subset of data which is used in the retrieval. Effects of the scan over the sun are visible.

The right column of Fig. 5 shows the selected transmissions after the corrections explained above, which now smoothly decrease with altitude as it is expected. The variation of transmission with altitude is different for each wavelength due to different absorbing and scattering effects. In general transmissions at shorter wavelengths are lower at lower altitudes mainly due to ozone absorption and stronger Rayleigh scattering. Below 10 km transmissions are close to zero due to the low input signal, which gives a lower limit for the later retrieval. At altitudes above about 30 km transmissions are close to one. Since extinction information is obtained from the difference of the transmission to one, this also implies an upper limit for the retrieval (see below).

The selected and corrected spectra are then fed into the ONPD retrieval (see section 4.1), in which the background polynomial is fitted considering gas absorptions and Rayleigh scattering. The results of this retrieval for orbit 8014 are shown in Fig. 6. The left column of this figures shows (again for the different extinction wavelengths):

- The corrected measured logarithmic transmission at 25 km (thick grey line).
- The SCIATRAN reference model spectrum for US standard atmosphere conditions, incl. Rayleigh scattering (green line).
- The model spectrum corrected for actual temperature, pressure and absorption of gases as derived from the fit (blue line).
- The fitted background polynomial (pink line).
- The fitted spectrum, i.e. the combination of the contributions of reference spectrum, absorption and polynomial (red line).

As the fit result (red) is very close to the measurement (grey) the right column of Fig. 6 shows the residual of both (measurement – fit), which is quite low (standard deviation below 0.002) indicating a good fit.

The white circles on the pink lines in Fig. 6 mark the value of the polynomial at the wavelength to be used for extinction retrieval. This is the value for 25 km; the complete profiles from 10 to 50 km are presented in the top of Fig. 7. These profiles



show the remaining transmission after effects of Rayleigh scattering and gas absorption have been subtracted. The difference to one can thus be interpreted as the effect of extinction.

270 The profiles of Fig. 7 are used as input for the extinction retrieval (see section 4.2). The resulting extinction profiles are given in Fig. 8. For comparison, we also plotted collocated SAGE II (at 452 and 525 nm) and SCIAMACHY limb aerosol extinction (at 750 nm) profiles. The error bars correspond to the error given in the product files. For SCIAMACHY occultation, this error is derived from the propagation of the transmission errors (Fig. 7 bottom). It does not consider any systematic contributions and is therefore only a lower estimate.

275 The overall agreement between SCIAMACHY occultation and SAGE II is quite good. Above about 30 km transmissions are close to one (see Fig. 7). Thus, SCIAMACHY occultation errors typically increase and the retrieved extinctions become very noisy. Furthermore, at higher altitudes vertical oscillations occur, which are artefacts probably introduced by the onion peeling method; similar effects have been seen in greenhouse gas retrievals (see e.g. Noël et al., 2018).

At 750 nm, the retrieved SCIAMACHY limb and aerosol extinctions are also quite similar. The vertical sampling of the  
280 limb data is however much sparser. Noise and error of the occultation data is smaller; oscillations at higher altitudes are more pronounced than at lower wavelengths. The extinction minimum in the limb data at about 15 km is not seen in the occultation data.

## 5.2 Validation

In this section we show the results of a comparison between the SCIAMACHY solar occultation V5.1.1 extinction data and  
285 corresponding profiles from the SAGE II V7.00A and the SCIAMACHY limb aerosol extinction product V1.4. Collocation criteria are in both cases 800 km / 9 h, resulting in 700 matches for SAGE II between 2002 and 2005 and 13435 matches with SCIAMACHY limb data between 2002 and 2012. For the comparisons, all extinction data are interpolated to the 1 km SCIAMACHY occultation data vertical grid.

Because of the larger random and/or systematic errors at higher altitudes (see previous subsection) we currently consider  
290 only SCIAMACHY solar occultation extinction data below 30 km as reliable. In addition, SCIAMACHY occultation data below about 15 km have to be treated with care, as e.g. the greenhouse gas occultation retrievals are known to give less accurate results there because of tropospheric influences not covered by the retrieval method (like increased refraction and strong vertical gradients at the tropopause). For the validation activities described in this section and later analyses we will therefore concentrate on the altitude range 15–30 km.

295 The results from the comparison with SAGE II at 452 and 525 nm are shown in Fig. 9.

Since extinctions exponentially decrease with altitude, mean differences and standard deviations of the differences decrease towards higher altitudes whereas relative differences increase. In general, there is no obvious bias between the SCIAMACHY occultation results and the correlative data sets visible, but especially at 452 nm the mean occultation profile shows an oscillation with altitude which is not present in the SAGE II data. This results in an oscillation of the differences with an amplitude  
300 of about 20–30% and an estimated period of about 10 km. For upper altitudes (above about 25 km) at 525 nm this oscillation even causes mean differences larger than 50% to SAGE II.



These kind of oscillating features have been observed in other ONPD products (see e.g. Noël et al., 2018). It is assumed that these are related to the onion peeling method which does not include e.g. regularisation on these vertical scales.

305 The mean error of the SCIAMACHY occultation product is at all wavelengths smaller than the standard deviation of the differences confirming that this error is indeed only a lower estimate. The standard deviation of the mean profiles is very similar for all comparisons. This indicates that all instruments / viewing geometries observe a comparable atmospheric variability.

For the comparison of SCIAMACHY occultation data with limb extinctions at 750 nm we divided the collocation data set into two parts corresponding to background conditions (defined by maximum extinctions below 0.001) and perturbed conditions (all others). The results are shown in Fig. 10.

310 Because of the large number of collocations the error of the mean difference is very small (dotted and solid red lines are almost on top of each other).

For the background case, the comparison reveals a very good agreement below 27 km within  $\pm 5\text{--}10\%$ . The standard deviations of the mean profiles are very similar for occultation and limb data, so variability is also comparable.

315 Under perturbed conditions, the atmospheric variability is much higher both in the spatial and temporal domain. The time offset of up to 10 h between occultation and limb measurements therefore results in a larger scatter between the two data sets and significantly increased standard deviations of differences and mean profiles of more than 100%. This is why the lower limit lines of the standard deviations are not always visible in the logarithmic profile plot (d). The variability for limb is even larger than for occultation, possibly because occultation measurements occur always at the same local time (sunset). However, the average agreement of the two data sets is very good between about 17 and 27 km.

320 Below 17 km deviations up to 50% are observed. This is in line with comparisons of OSIRIS and SCIAMACHY limb extinctions with SAGE II data (Rieger et al., 2018), which also revealed discrepancies of similar magnitude and sign at higher latitudes. It is assumed that these differences are due to the assumptions on particle sizes made in the limb retrievals, which are most crucial for high Northern latitudes because of low scattering angles.

325 Above 27 km deviations increase with occultation data being typically larger. This is most likely also related to oscillations in the occultation profiles (see Fig. 8).

## 6 Time series

### 6.1 Extinction time series

330 The complete time series of SCIAMACHY solar occultation data has been processed for the three extinction wavelengths investigated in the present study. After filtering out invalid data (from times of non-nominal instrument performance, e.g. during decontamination periods) in total 43686 profiles (from August 2002 to April 2012) remained, from which daily average extinction profiles were created. Because of the sun fixed ENVISAT orbit, all measurements of one day occur at essentially the same latitude but different longitudes. Thus, the geographic latitude of the measurements varies systematically with season and the daily averages are also zonal means (see also Noël et al., 2018). Higher latitudes ( $\sim 65\text{--}70^\circ$ ) typically occur in winter and lower latitudes ( $\sim 50\text{--}60^\circ$ ) in summer.



335 Fig. 11 shows the resulting gridded time series from August 2002 to April 2012 for 452 nm, 525 nm and 750 nm (top to  
bottom plots) from 15 to 30 km. The colour scale is logarithmic accounting for the typical exponential decrease of the extinction  
with altitude which is clearly visible in this figure at all wavelengths.

After 2008 there are some pronounced increases of extinction up to about 0.01 at lower altitudes visible. These are caused  
be the eruption of volcanoes at higher latitudes (marked by arrows) which reached into the stratosphere. The sudden increase  
340 due to upward transport of aerosol particles directly after the eruption is then followed by a gradually downward transport and  
decrease of extinction taking several months up to one year. This can be seen at all wavelengths.

The observed extinctions also vary with season, which is partly caused by the systematic coupling between time and latitude  
mentioned above and the related variations in tropopause height.

## 6.2 Anomalies

345 To further investigate the temporal behaviour and to reduce the influence of possible systematic features in the data (e.g. vertical  
oscillations, see above) we computed monthly relative anomalies of the extinction. We concentrate here on the years 2003 to  
2011 to avoid possible influences of missing months in the first and the last year on the weighting of data points.

For this, we first generated for each altitude monthly means from the daily average profiles. From these monthly averages  
we then subtracted the 2003 to 2006 average value for each month to obtain absolute anomaly profiles. These data are then  
350 divided by the mean of the monthly average extinction profiles from 2003 to 2006 to remove the overall vertical shape of the  
extinction profiles (especially the exponential decrease with altitude). We do not use data after 2006 to determine the mean  
extinction profiles to avoid influences of the prominent volcanic eruptions at lower altitudes (as seen in Fig. 11). The reference  
for the anomalies can therefore be interpreted as a “background time” mean.

The resulting relative anomalies may then be plotted using a common linear scale for all altitudes which facilitates the  
355 interpretation of the data. As already seen in the extinction plots (Fig. 11) extinctions increased during times of volcanic  
influences by more than a factor of 10. These events are of course also clearly visible in the relative anomalies, but here we  
want to focus on smaller effects which cannot directly be inferred from the extinction time series. Therefore we concentrate  
on the range of relative anomalies between  $\pm 4$ . Fig. 12 shows the monthly relative anomalies generated by the procedure  
described above using this scale.

360 Below 20 km, in addition to the three periods of volcanic influences after mid 2008 the “background time” before 2007 can  
be clearly identified. During this time interval relative anomalies are close to zero, but slightly increasing with time.

Especially at the lower wavelengths a small increase of relative extinction anomaly at the beginning of 2007 is observed.  
This is related to the influence of volcanic eruptions in the tropical region in 2006 (Soufrière Hills, Tavurvur) and later transport  
of particles to higher latitudes (see e.g. von Savigny et al., 2015).

365 The 525 nm data show during January 2007 an oscillating structure between 16 and 19 km. In fact, this feature is visible  
with different strength at all wavelengths. It is most likely induced by the presence of strong Polar Stratospheric Clouds (PSCs)  
partly blocking the measured signal below 20 km, which is supported by the time and location of the measurements (high  
latitudes in winter) and ECMWF data showing during this month at these altitudes temperatures below 195 K at which PSCs



can be formed. In fact, the 750 nm plot shows several enhancements in winter time (e.g. in January 2008, 2010 and 2011)  
370 between 20 and 30 km which we attribute to (in these cases less strong) PSCs. The occurrence of PSCs at altitudes up to  
30 km in January 2011 is quite unusual. It is confirmed also by CALIOP and MIPAS measurements and related to specific  
meteorological conditions during this winter leading e.g. to a record ozone loss (see e.g. Arnone et al., 2012; Khosrawi et al.,  
2016; Pitts et al., 2018).

Altitudes above 25 km show a regular pattern of alternating positive and negative anomalies with a period of about two  
375 years. As e.g. shown in Noël et al. (2018) this temporal variation is a transport effect assumed to be associated with the  
Quasi-Biennial-Oscillation (QBO), see e.g. Baldwin et al. (2001).

Similar features can be seen in Fig. 13, which shows relative anomalies of the SCIAMACHY limb extinction data as function  
of altitude and time. This plot is based on the complete set of about 40000 collocated limb profiles used in the comparisons  
above (see section 5.2). These limb data have been processed the same way as the occultation data to yield the anomalies.

380 The results for the limb extinctions are indeed very similar to occultation, but because of the larger variability of the limb  
data PSCs are more frequently visible in winter time. Anomalies are also somewhat larger for volcanic events, which is in line  
with the validation results.

To further illustrate this, Fig. 14 shows corresponding time series at 15, 20 and 25 km. Whereas the overall agreement of  
the temporal behaviour of the limb and occultation data sets is very good, individual events (PSCs, volcanic eruptions) are  
385 sometimes differently pronounced due to different measurement times and locations.

Based on the relative anomaly profiles we have determined linear changes for the temporal range 2003 to 2011 by fitting  
a straight line to the time series for each altitude. The results for 452 nm, 525 nm and 750 nm are displayed in Fig. 15. All  
changes are given relative to the “background time” mean of the extinction between 2003 and 2006 as mentioned above.  
Changes smaller than the  $2\sigma$  error derived from the fit (indicated by shaded areas around the lines) are considered to be  
390 insignificant. The results are quite similar for all wavelengths and also for limb data (green) and occultation data (red).

At 15 km a significant positive change of 20–30% per year is derived, which decreases with increasing altitude and becomes  
insignificant above about 22–25 km. Obviously, this change at lower altitudes is mainly determined by the increased extinctions  
due to the volcanic eruptions during the second half of the time series (see Fig. 14). Higher altitudes are mainly affected by  
QBO related variations which mostly average out.

## 395 7 Conclusions

Based on an improved radiometric calibration of SCIAMACHY solar occultation measurements and a newly developed onion  
peeling retrieval method a stratospheric extinction profiles data set at 452 nm, 525 nm and 750 nm for the time interval August  
2002 to April 2012 could be derived. This data set covers the latitudinal region between about 50°N and 70°N at a specific  
spatial/temporal sampling. Reasonable results are obtained between 15 km and 30 km.

400 Comparisons with SAGE II data products show a good agreement with essentially no mean bias but altitude dependent  
differences in the order of 20–30%. These differences are mainly due to unexpected vertical oscillations in the SCIAMACHY



extinction profiles with a period of about 10 km. It is assumed that these oscillations are caused by the onion peeling retrieval method, as similar effects have been seen in the analysis of greenhouse gas profiles derived from SCIAMACHY solar occultation measurements (Noël et al., 2018). The overall agreement with SCIAMACHY limb data at 750 nm is quite good between  
405 about 17 and 27 km (5–10%). At higher and lower altitudes deviations up to about 50% are observed, which are caused by oscillations in the occultation data (above 27 km) and deficiencies of the limb data at higher latitudes (below 17 km). The scatter in the data is especially large during perturbed / high aerosol load conditions.

Time series of SCIAMACHY solar occultation extinctions and related anomalies show the expected influences of major volcanic eruptions reaching the stratosphere, which cause a sudden increase of extinction by one magnitude or more below  
410 20 km followed by a gradually decrease / downward transport over several months. Furthermore, some enhanced extinctions during polar winter time were detected between 20 and 30 km which are attributed to the presence of PSCs.

A systematic variation of extinctions with season is observed, which is caused by the spatial/temporal coupling of the SCIAMACHY solar occultation measurements resulting in a regular variation of the tropopause height over the year. At altitudes above 25 km also QBO effects are seen, which is in line with the results of greenhouse gas studies (Noël et al., 2018).

415 Vertical profiles of linear changes derived from extinction anomalies show significant positive changes of up to 20–30% per year for the time interval 2003 to 2011 at 15 km. These changes are given relative to atmospheric background aerosol conditions, which have been estimated from the period 2003 to 2006 when no major volcanic eruptions were present above 50°N. The overall extinction increase from 2003 to 2011 is mainly caused by the volcanic eruptions occurring in the second half of the time series.

420 These results show, that the new SCIAMACHY solar occultation extinction data products are of reasonable quality and useful for geophysical interpretations. As for the corresponding greenhouse gas data the quality of the products seems to be mainly limited by systematic effects, especially by vertical oscillations at altitudes above 30 km.

## Appendix A: Azimuth correction

Switching to the sun follower (SF) in azimuth at about 17 km tangent height may result in different azimuthal positions of  
425 the IFOV before/after the switch, resulting in a jump of the measured signal to a higher value. Azimuth mispointing may also occur due to a mismatch between the predicted (commanded) and true sun position. This is only critical, if the angular shift is so large that part of the sun is not inside IFOV (see right plot in Fig.2). The effect on the signal due to this missing area can be corrected using the known position of the IFOV on the sun (see above), but this requires the knowledge about the width of the IFOV. Unfortunately, there is not much information from SCIAMACHY on-ground calibration about the IFOV in solar  
430 occultation geometry, because this uses a smaller aperture than in the standard Earthshine measurements. This small aperture reduces the light by 3–4 orders of magnitude, which makes measurements with typical on-ground light sources difficult as they would require long integration times. Usually, a typical value of 0.72° is given for the small aperture IFOV width (see e.g. Gottwald and Bovensmann, 2011).



To investigate the impact of azimuthal jumps in the signal after switching on the SF on the final aerosol product we looked  
435 at discontinuities in the retrieved extinctions around 17 km as function of IFOV width. It turned out that only data a few  
kilometres around 17 km are affected by the azimuth jumps. Smoothest profiles are achieved when assuming an IFOV width  
of 0.68°, which is why we used this value in our study.

## Appendix B: Bending angle fit

The underlying assumption for the determination of the bending angle is that the atmosphere does not change during one  
440 occultation measurement. This, however, is a general assumption of the retrieval method. The bending angle can then be  
determined using the fact that altitudes of adjacent upward/downward scans overlap. This is illustrated in Fig. A1, which  
shows as example the (uncorrected) measured transmissions  $T_1^m$  and  $T_2^m$  of two upward scans (nos. 18 and 20). These two  
measurements are centred around different tangent heights, but the covered altitude ranges overlap. Let  $P_1$  be the point where  
the transmission of scan 18 is highest. This occurs at a tangent altitude  $z_1$  of about 33.5 km. If we interpolate the transmissions  
445 of scan 20 to this altitude, we get point  $P_2$ . The points  $(P_1, P_2)$  therefore correspond to an observation of the same tangent  
altitude, but for different viewing directions  $(\gamma_1, \gamma_2)$  and for different sun positions  $(\beta_1, \beta_2)$ . Since the observed point in the  
atmosphere is the same, the scan-corrected transmissions should also be the same, i.e.:

$$T_1(z_1) = T_2(z_1) \quad (\text{B1})$$

The fact that we observe different transmissions ( $T_1^m(z_1) > T_2^m(z_1)$ ) is due to refraction, i.e. the (same) bending angle  $\delta(z_1)$   
450 at this altitude.

Combining Eqs. (B1) and (3) leads to:

$$\frac{T_1^m(z_1)}{T_2^m(z_1)} = \frac{S(\gamma_1 - \beta_1 - \delta(z_1))}{S(\gamma_2 - \beta_2 - \delta(z_1))} \quad (\text{B2})$$

This equation can be solved numerically to derive  $\delta(z_1)$ . In principle, this procedure can be applied to all pairs of scans;  
however, it is practically limited by the low transmissions at lower altitudes and too small refraction at higher altitudes. We  
455 therefore restrict the application to the altitude range 15 to 35 km, which gives us about five data points of  $\delta$  for different  
tangent altitudes  $z$ .

We then fit a straight line to  $\log \delta(z)$  to derive the parameters  $a$  and  $b$  from Eq. 1. This is done independently for each  
considered wavelength. An example for this is show in Fig. A2.

*Data availability.* The SCIAMACHY solar occultation extinction data presented in this work (V5.1.1) are available on request from the  
460 authors.





*Author contributions.* SN developed the calibration and retrieval methods, generated the SCIAMACHY occultation extinction data set and performed the analysis of the data. KB provided the pointing corrections for the data. AR and EM produced the SCIAMACHY limb extinction data set. All authors (incl. HB and JPB) contributed to the preparation of the manuscript.

*Competing interests.* The authors declare that they have no conflict of interest.

465 *Acknowledgements.* SCIAMACHY data have been provided by ESA. We thank the European Center for Medium Range Weather Forecasts (ECMWF) for providing us with analysed meteorological fields. SAGE II data were obtained from the NASA Langley Research Center Atmospheric Science Data Center. This work has been funded by DLR-Bonn (SADOS-III project), by ESA (SQWG-III project), by the University of Bremen and partially by DFG through the research unit VolImpact.



## References

- 470 Arnone, E., Castelli, E., Papandrea, E., Carlotti, M., and Dinelli, B. M.: Extreme ozone depletion in the 2010–2011 Arctic winter stratosphere as observed by MIPAS/ENVISAT using a 2-D tomographic approach, *Atmos. Chem. Phys.*, 12, 9149–9165, <https://doi.org/10.5194/acp-12-9149-2012>, <https://www.atmos-chem-phys.net/12/9149/2012/>, 2012.
- Baldwin, M. P., Gray, L. J., Dunkerton, T. J., Hamilton, K., Haynes, P. H., Randel, W. J., Holton, J. R., Alexander, M. J., Hirota, I., Horinouchi, T., Jones, D. B. A., Kinnersley, J. S., Marquardt, C., Sato, K., and Takahashi, M.: The quasi-biennial oscillation, *Reviews of Geophysics*,
- 475 39, 179–229, <https://doi.org/10.1029/1999RG000073>, <http://dx.doi.org/10.1029/1999RG000073>, 2001.
- Bevilacqua, R. M., Hoppel, K. W., Hornstein, J. S., Lucke, R. L., Shettle, E. P., Ainsworth, T. L., Debrestian, D., Fromm, M. D., Krigman, S. S., Lumpe, J., Glaccum, W., Olivero, J. J., Clancy, R. T., Randall, C. E., Rusch, D. W., Chassefière, E., Dalaudier, F., Deniel, C., Brogniez, C., and Lenoble, J.: First results from POAM II: The dissipation of the 1993 Antarctic Ozone Hole, *Geophys. Res. Lett.*, 22, 909–912, <https://doi.org/10.1029/95GL00535>, <https://agupubs.onlinelibrary.wiley.com/doi/abs/10.1029/95GL00535>, 1995.
- 480 Bourassa, A. E., Rieger, L. A., Lloyd, N. D., and Degenstein, D. A.: Odin-OSIRIS stratospheric aerosol data product and SAGE III intercomparison, *Atmos. Chem. Phys.*, 12, 605–614, <https://doi.org/10.5194/acp-12-605-2012>, <https://www.atmos-chem-phys.net/12/605/2012/>, 2012.
- Bramstedt, K., Stone, T. C., Gottwald, M., Noël, S., Bovensmann, H., and Burrows, J. P.: Improved pointing information for SCIAMACHY from in-flight measurements of the viewing directions towards sun and moon, *Atmos. Meas. Tech.*, 10, 2413–2423,
- 485 <https://doi.org/10.5194/amt-10-2413-2017>, <https://www.atmos-meas-tech.net/10/2413/2017/>, 2017.
- Chen, Z., Bhartia, P. K., Loughman, R., Colarco, P., and DeLand, M.: Improvement of stratospheric aerosol extinction retrieval from OMPS/LP using a new aerosol model, *Atmos. Meas. Tech.*, 11, 6495–6509, <https://doi.org/10.5194/amt-11-6495-2018>, <https://www.atmos-meas-tech.net/11/6495/2018/>, 2018.
- Chu, W. P. and McCormick, M. P.: Inversion of stratospheric aerosol and gaseous constituents from spacecraft solar extinction data in the
- 490 0.38–1.0- $\mu\text{m}$  wavelength region, *Appl. Optics*, 18, 1979.
- Cisewski, M., Zawodny, J., Gasbarre, J., Eckman, R., Topiwala, N., Rodriguez-Alvarez, O., Cheek, D., and Hall, S.: The Stratospheric Aerosol and Gas Experiment (SAGE III) on the International Space Station (ISS) Mission, in: *Sensors, Systems, and Next-Generation Satellites XVIII*, edited by Meynart, R., Neeck, S. P., and Shimoda, H., vol. 9241, pp. 59 – 65, International Society for Optics and Photonics, SPIE, <https://doi.org/10.1117/12.2073131>, <https://doi.org/10.1117/12.2073131>, 2014.
- 495 Coldewey-Egbers, M., Weber, M., Lamsal, L. N., de Beek, R., Buchwitz, M., and Burrows, J. P.: Total ozone retrieval from GOME UV spectral data using the weighting function DOAS approach, *Atmospheric Chemistry and Physics*, 5, 1015–1025, <https://doi.org/10.5194/acp-5-1015-2005>, <http://www.atmos-chem-phys.net/5/1015/2005/>, 2005.
- Damadeo, R. P., Zawodny, J. M., Thomason, L. W., and Iyer, N.: SAGE version 7.0 algorithm: application to SAGE II, *Atmos. Meas. Tech.*, 6, 3539–3561, <https://doi.org/10.5194/amt-6-3539-2013>, <https://www.atmos-meas-tech.net/6/3539/2013/>, 2013.
- 500 Dee, D. P., Uppala, S. M., Simmons, A. J., Berrisford, P., Poli, P., Kobayashi, S., Andrae, U., Balmaseda, M. A., Balsamo, G., Bauer, P., Bechtold, P., Beljaars, A. C. M., van de Berg, L., Bidlot, J., Bormann, N., Delsol, C., Dragani, R., Fuentes, M., Geer, A. J., Haimberger, L., Healy, S. B., Hersbach, H., Hólm, E. V., Isaksen, I., Kållberg, P., Köhler, M., Matricardi, M., McNally, A. P., Monge-Sanz, B. M., Morcrette, J.-J., Park, B.-K., Peubey, C., de Rosnay, P., Tavolato, C., Thépaut, J.-N., and Vitart, F.: The ERA-Interim reanalysis: configuration and performance of the data assimilation system, *Quart. Jour. R. Met. Soc.*, 137, 553–597, <https://doi.org/10.1002/qj.828>, <http://dx.doi.org/10.1002/qj.828>, 2011.
- 505



- Fischer, H., Birk, M., Blom, C., Carli, B., Carlotti, M., von Clarmann, T., Delbouille, L., Dudhia, A., Ehhalt, D., Endemann, M., Flaud, J. M., Gessner, R., Kleinert, A., Koopman, R., Langen, J., López-Puertas, M., Mosner, P., Nett, H., Oelhaf, H., Perron, G., Remedios, J., Ridolfi, M., Stiller, G., and Zander, R.: MIPAS: an instrument for atmospheric and climate research, *Atmos. Chem. Phys.*, 8, 2151–2188, <http://www.atmos-chem-phys.net/8/2151/2008/>, 2008.
- 510 Gottwald, M. and Bovensmann, H., eds.: *SCIAMACHY - Exploring the Changing Earth's Atmosphere*, Springer Dordrecht Heidelberg London New York, <https://doi.org/10.1007/978-90-481-9896-2>, 2011.
- Jaross, G., Bhartia, P. K., Chen, G., Kowitt, M., Haken, M., Chen, Z., Xu, P., Warner, J., and Kelly, T.: OMPS Limb Profiler instrument performance assessment, *J. Geophys. Res. Atmos.*, 119, 4399–4412, <https://doi.org/10.1002/2013JD020482>, <https://agupubs.onlinelibrary.wiley.com/doi/abs/10.1002/2013JD020482>, 2014.
- 515 Kent, G. S. and McCormick, M. P.: SAGE and SAM II Measurements of Global Stratospheric Aerosol Optical Depth and Mass Loading, *J. Geophys. Res.*, 89, 5303–5314, 1984.
- Khosrawi, F., Urban, J., Lossow, S., Stiller, G., Weigel, K., Braesicke, P., Pitts, M. C., Rozanov, A., Burrows, J. P., and Murtagh, D.: Sensitivity of polar stratospheric cloud formation to changes in water vapour and temperature, *Atmospheric Chemistry and Physics*, 16, 101–121, <https://doi.org/10.5194/acp-16-101-2016>, <https://www.atmos-chem-phys.net/16/101/2016/>, 2016.
- 520 Kyrölä, E., Tamminen, J., Sofieva, V., Bertaux, J. L., Hauchecorne, A., Dalaudier, F., Fussen, D., Vanhellemont, F., Fanton d'Andon, O., Barrot, G., Guirlet, M., Mangin, A., Blanot, L., Fehr, T., Saavedra de Miguel, L., and Fraisse, R.: Retrieval of atmospheric parameters from GOMOS data, *Atmos. Chem. Phys.*, 10, 11 881–11 903, <https://doi.org/10.5194/acp-10-11881-2010>, <https://www.atmos-chem-phys.net/10/11881/2010/>, 2010.
- Lee, K.-M., Park, J. H., Massie, S. T., and Choi, W.: Extinction coefficients and properties of Pinatubo aerosol determined from Halogen Occultation Experiment (HALOE) data, *J. Geophys. Res. Atmos.*, 106, 28 333–28 345, <https://doi.org/10.1029/2000JD000251>, <https://agupubs.onlinelibrary.wiley.com/doi/abs/10.1029/2000JD000251>, 2001.
- Llewellyn, E. J., Lloyd, N. D., Degenstein, D. A., Gattinger, R. L., Petelina, S. V., Bourassa, A. E., Wiensz, J. T., Ivanov, E. V., McDade, I. C., Solheim, B. H., McConnell, J. C., Haley, C. S., von Savigny, C., Sioris, C. E., McLinden, C. A., Griffioen, E., Kaminski, J., Evans, W. F., Puckrin, E., Strong, K., Wehrle, V., Hum, R. H., Kendall, D. J., Matsushita, J., Murtagh, D. P., Brohede, S., Stegman, J., Witt, G., Barnes, G., Payne, W. F., Piché, L., Smith, K., Warshaw, G., Deslauniers, D. L., Marchand, P., Richardson, E. H., King, R. A., Wevers, I., McCreath, W., Kyrölä, E., Oikarinen, L., Leppelmeier, G. W., Auvinen, H., Mégie, G., Hauchecorne, A., Lefèvre, F., de La Nöe, J., Ricard, P., Frisk, U., Sjöberg, F., von Schéele, F., and Nordh, L.: The OSIRIS instrument on the Odin spacecraft, *Can. J. Phys.*, 82, 411–422, <https://doi.org/10.1139/p04-005>, <https://doi.org/10.1139/p04-005>, 2004.
- 530 Loughman, R., Bhartia, P. K., Chen, Z., Xu, P., Nyaku, E., and Taha, G.: The Ozone Mapping and Profiler Suite (OMPS) Limb Profiler (LP) Version 1 aerosol extinction retrieval algorithm: theoretical basis, *Atmos. Meas. Tech.*, 11, 2633–2651, <https://doi.org/10.5194/amt-11-2633-2018>, <https://www.atmos-meas-tech.net/11/2633/2018/>, 2018.
- Malinina, E., Rozanov, A., Rozanov, V., Liebing, P., Bovensmann, H., and Burrows, J. P.: Aerosol particle size distribution in the stratosphere retrieved from SCIAMACHY limb measurements, *Atmos. Meas. Tech.*, 11, 2085–2100, <https://doi.org/10.5194/amt-11-2085-2018>, <https://www.atmos-meas-tech.net/11/2085/2018/>, 2018.
- 540 Malinina, E., Rozanov, A., Rieger, L., Bourassa, A., Bovensmann, H., Burrows, J. P., and Degenstein, D.: Stratospheric aerosol characteristics from space-borne observations: extinction coefficient and Ångström exponent, *Atmos. Meas. Tech.*, 12, 3485–3502, <https://doi.org/10.5194/amt-12-3485-2019>, <https://www.atmos-meas-tech.net/12/3485/2019/>, 2019.
- McCormick, M. P.: SAGE II: An overview, *Adv. Space Res.*, 7, (3)219–(3)226, 1987.



- NASA: U.S. Standard Atmosphere Supplements, Tech. rep., U.S. Government Printing Office, Washington, D.C., 1976.
- 545 Noël, S., Bramstedt, K., Rozanov, A., Bovensmann, H., and Burrows, J. P.: Water vapour profiles from SCIAMACHY solar occultation measurements derived with an onion peeling approach, *Atmos. Meas. Tech.*, 3, 523–535, <http://www.atmos-meas-tech.net/3/523/2010/>, 2010.
- Noël, S., Bramstedt, K., Rozanov, A., Bovensmann, H., and Burrows, J. P.: Stratospheric methane profiles from SCIAMACHY solar occultation measurements derived with onion peeling DOAS, *Atmos. Meas. Tech.*, 4, 2567–2577, <https://doi.org/10.5194/amt-4-2567-2011>,  
550 <http://www.atmos-meas-tech.net/4/2567/2011/>, 2011.
- Noël, S., Bramstedt, K., Hilker, M., Liebing, P., Plieninger, J., Reuter, M., Rozanov, A., Sioris, C. E., Bovensmann, H., and Burrows, J. P.: Stratospheric CH<sub>4</sub> and CO<sub>2</sub> profiles derived from SCIAMACHY solar occultation measurements, *Atmos. Meas. Tech.*, 9, 1485–1503, <https://doi.org/10.5194/amt-9-1485-2016>, <http://www.atmos-meas-tech.net/9/1485/2016/>, 2016.
- Noël, S., Weigel, K., Bramstedt, K., Rozanov, A., Weber, M., Bovensmann, H., and Burrows, J. P.: Water vapour and methane  
555 coupling in the stratosphere observed using SCIAMACHY solar occultation measurements, *Atmos. Chem. Phys.*, 18, 4463–4476, <https://doi.org/10.5194/acp-18-4463-2018>, <https://www.atmos-chem-phys.net/18/4463/2018/>, 2018.
- Osborn, M. T., Rosen, J. M., McCormick, M. P., Wang, P.-H., Livingston, J. M., and Swissler, T. J.: SAGE II Aerosol Correlative Observations: Profile Measurements, *J. Geophys. Res.*, 94, 8353–8366, 1989.
- Pitts, M. C., Poole, L. R., and Gonzalez, R.: Polar stratospheric cloud climatology based on CALIPSO spaceborne lidar measurements  
560 from 2006 to 2017, *Atmospheric Chemistry and Physics*, 18, 10 881–10 913, <https://doi.org/10.5194/acp-18-10881-2018>, <https://www.atmos-chem-phys.net/18/10881/2018/>, 2018.
- Randall, C. E., Rusch, D. W., Olivero, J. J., Bevilacqua, R. M., Poole, L. R., Lumpe, J. D., Fromm, M. D., Hoppel, K. W., Hornstein, J. S., and Shettle, E. P.: An overview of POAM II aerosol measurements at 1.06  $\mu\text{m}$ , *Geophys. Res. Lett.*, 23, 3195–3198, <https://doi.org/10.1029/96GL02921>, <https://agupubs.onlinelibrary.wiley.com/doi/abs/10.1029/96GL02921>, 1996.
- 565 Randel, W. J., Park, M., Emmons, L., Kinnison, D., Bernath, P., Walker, K. A., Boone, C., and Pumphrey, H.: Asian Monsoon Transport of Pollution to the Stratosphere, *Science*, 328, 611–613, <https://doi.org/10.1126/science.1182274>, <https://science.sciencemag.org/content/328/5978/611>, 2010.
- Rieger, L. A., Bourassa, A. E., and Degenstein, D. A.: Stratospheric aerosol particle size information in Odin-OSIRIS limb scatter spectra, *Atmos. Meas. Tech.*, 7, 507–522, <https://doi.org/10.5194/amt-7-507-2014>, <https://www.atmos-meas-tech.net/7/507/2014/>, 2014.
- 570 Rieger, L. A., Malinina, E. P., Rozanov, A. V., Burrows, J. P., Bourassa, A. E., and Degenstein, D. A.: A study of the approaches used to retrieve aerosol extinction, as applied to limb observations made by OSIRIS and SCIAMACHY, *Atmos. Meas. Tech.*, 11, 3433–3445, <https://doi.org/10.5194/amt-11-3433-2018>, <https://www.atmos-meas-tech.net/11/3433/2018/>, 2018.
- Rieger, L. A., Zawada, D. J., Bourassa, A. E., and Degenstein, D. A.: A Multiwavelength Retrieval Approach for Improved OSIRIS Aerosol Extinction Retrievals, *J. Geophys. Res. Atmos.*, 124, 7286–7307, <https://doi.org/10.1029/2018JD029897>, <https://agupubs.onlinelibrary.wiley.com/doi/abs/10.1029/2018JD029897>, 2019.
- 575 Rozanov, V. V., Rozanov, A. V., Kokhanovsky, A. A., and Burrows, J. P.: Radiative transfer through terrestrial atmosphere and ocean: Software package SCIATRAN, *J. Quant. Spectr. Rad. Transf.*, <https://doi.org/10.1016/j.jqsrt.2013.07.004>, <http://www.sciencedirect.com/science/article/pii/S0022407313002872>, 2013.
- Russell, III, J. M., Gordley, L. L., Park, J. H., Drayson, S. R., Hesketh, W. D., Cicerone, R. J., Tuck, A. F., Frederick, J. E., Harries, J. E., and  
580 Crutzen, P. J.: The Halogen Occultation Experiment, *J. Geophys. Res.*, 98, 10 777–10 797, 1993.



- Russell, P. B. and McCormick, M. P.: SAGE II Aerosol Data Validation and Initial Data Use: An Introduction and Overview, *J. Geophys. Res.*, 94, 8335–8338, 1989.
- Thomason, L. W. and Taha, G.: SAGE III aerosol extinction measurements: Initial results, *J. Geophys. Res.*, 30, 1631, <https://doi.org/10.1029/2003GL017317>, 2003.
- 585 Thomason, L. W., Burton, S. P., Luo, B.-P., and Peter, T.: SAGE II measurements of stratospheric aerosol properties at non-volcanic levels, *Atmos. Chem. Phys.*, 8, 983–995, <https://doi.org/10.5194/acp-8-983-2008>, <https://www.atmos-chem-phys.net/8/983/2008/>, 2008.
- Vernier, J.-P., Thomason, L. W., and Kar, J.: CALIPSO detection of an Asian tropopause aerosol layer, *Geophys. Res. Lett.*, 38, <https://doi.org/10.1029/2010GL046614>, <https://agupubs.onlinelibrary.wiley.com/doi/abs/10.1029/2010GL046614>, 2011.
- 590 von Savigny, C., Ernst, F., Rozanov, A., Hommel, R., Eichmann, K.-U., Rozanov, V., Burrows, J. P., and Thomason, L. W.: Improved stratospheric aerosol extinction profiles from SCIAMACHY: validation and sample results, *Atmos. Meas. Tech.*, 8, 5223–5235, <https://doi.org/10.5194/amt-8-5223-2015>, <https://www.atmos-meas-tech.net/8/5223/2015/>, 2015.
- Winker, D. M., Hunt, W. H., and McGill, M. J.: Initial performance assessment of CALIOP, *Geophys. Res. Lett.*, 34, <https://doi.org/10.1029/2007GL030135>, <https://agupubs.onlinelibrary.wiley.com/doi/abs/10.1029/2007GL030135>, 2007.



**Table 1.** Satellite measurements of stratospheric aerosols.

Instrument	Platform	Measurement Time	Viewing Geometry
SAM	Apollo-Soyuz	1975	solar occultation
SAM-II	Nimbus-7	1978 – 1993	solar occultation
SAGE-I	AEM-B	1979 – 1981	solar occultation
SAGE II	ERBS	1984 – 2005	solar occultation
SAGE III	Meteor-3M	2001 – 2006	solar occultation
HALOE	UARS	1991 – 2001	solar occultation
POAM-II	SPOT-3	1993 – 1996	solar occultation
POAM-III	SPOT-4	1998 – 2005	solar occultation
GOMOS	ENVISAT	2002 – 2012	stellar occultation
MIPAS	ENVISAT	2002 – 2012	limb
SCIAMACHY	ENVISAT	2002 – 2012	nadir, limb, solar & lunar occultation
OSIRIS	Odin	since 2001	limb
CALIOP	CALIPSO	since 2006	nadir
OMPS	Suomi NPP	since 2011	nadir/limb
SAGE III	ISS	since 2017	solar occultation



**Table 2.** Sequence and settings of ONPD retrieval.

Sequence No.	$\lambda_{\text{ext}}$	Fit interval	Considered absorbers (source/fit)			
1	525 nm	510 – 580 nm	pressure (ECMWF)	temperature (ECMWF)	O <sub>3</sub> (Fit)	NO <sub>2</sub> (Fit)
2	452 nm	440 – 460 nm	pressure (ECMWF)	temperature (ECMWF)	O <sub>3</sub> (525 nm)	NO <sub>2</sub> (525 nm)
3	750 nm	750 – 758 nm	pressure (ECMWF)	temperature (ECMWF)	O <sub>3</sub> (525 nm)	



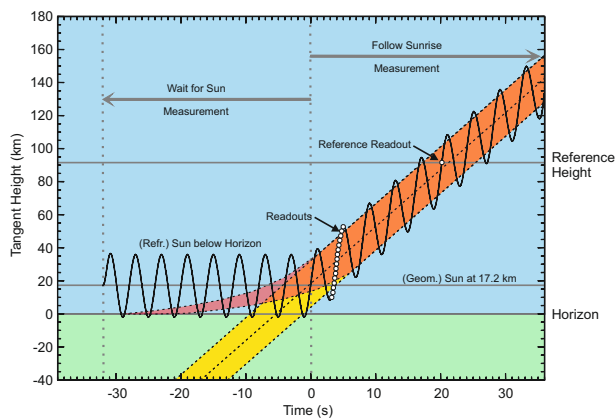


Figure 1. SCIAMACHY solar occultation measurement (figure from Noël et al., 2016).

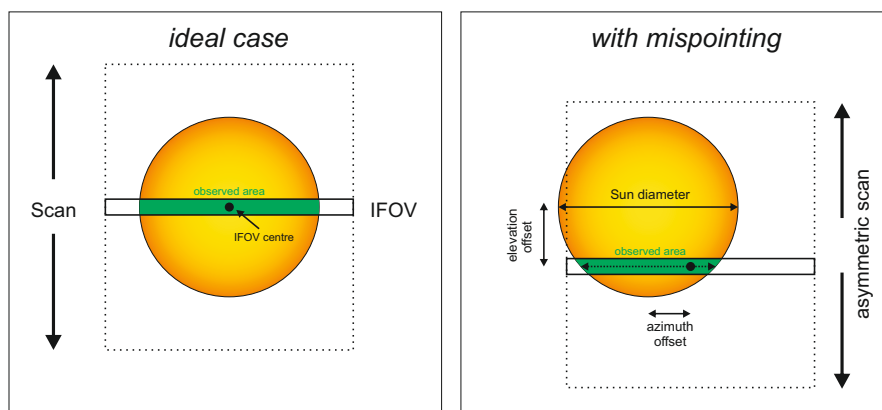
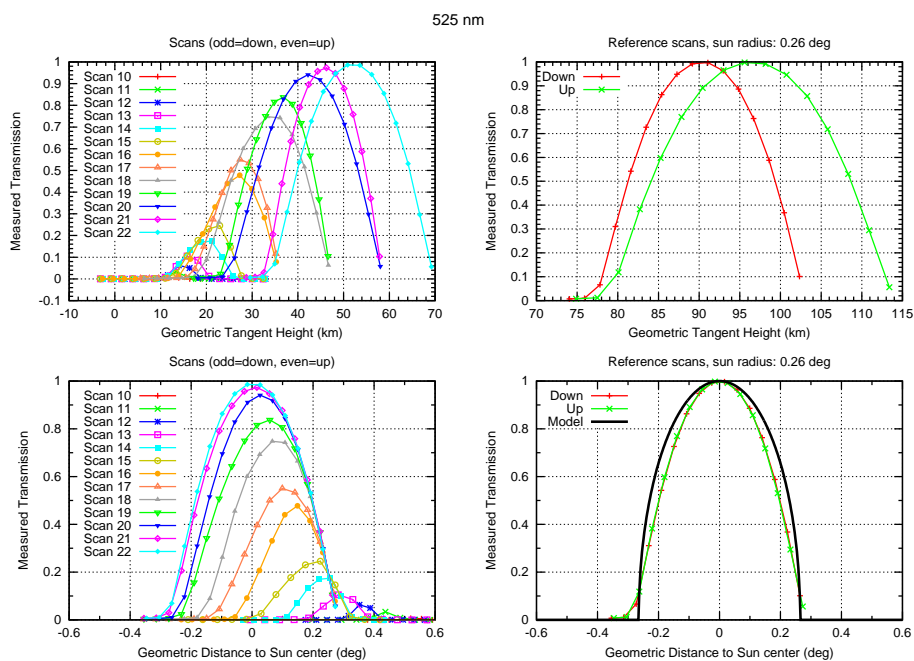
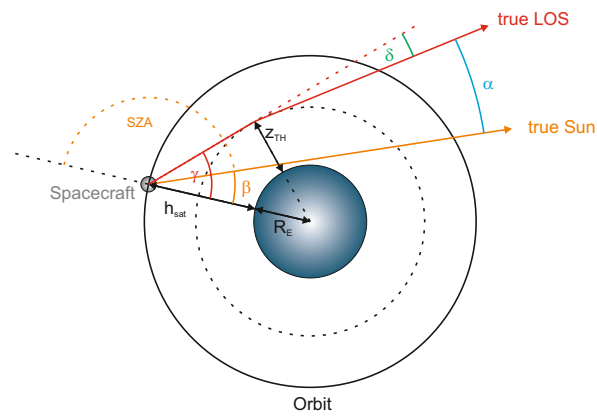


Figure 2. SCIAMACHY instantaneous field of view (IFOV) while scanning over the sun. Left: Ideal case (sun in centre of IFOV). Right: With mispointing (shift between centres of sun and IFOV); this is actually the nominal case.



**Figure 3.** SCIAMACHY transmission spectra at 525 nm. Top left: Measured transmission as function of tangent altitude for different scans. Top right: Reference transmissions as function of tangent altitude for up- and downscan. Bottom left: Measured transmission as function of distance to sun centre. Bottom right: Transmissions as function of distance to sun centre and corresponding model.



**Figure 4.** Definition of angles and other quantities used in the refraction model.

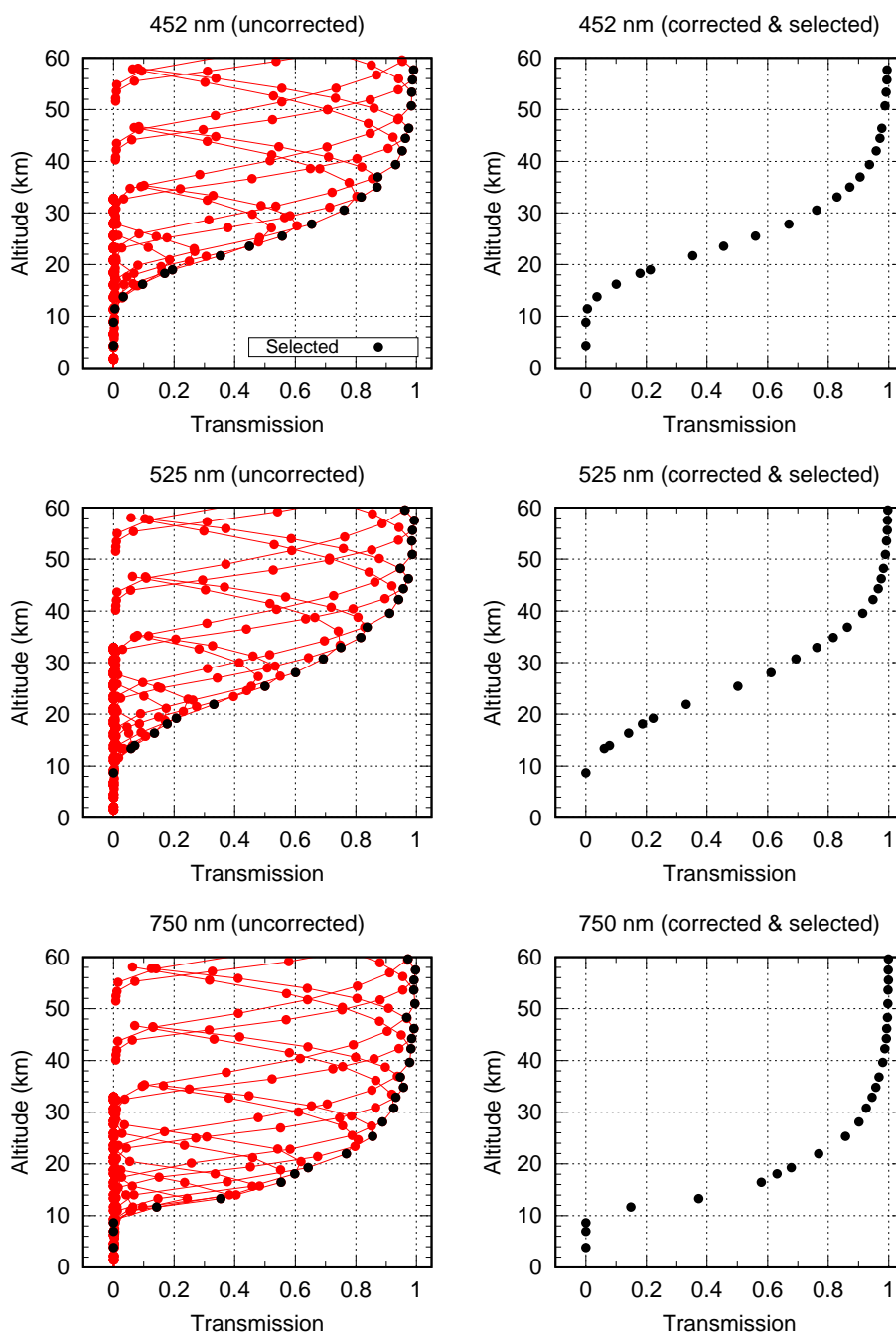


**Figure 5.** Transmissions for orbit 8014 (11 September 2003) and different wavelengths (top to bottom). Left: Uncorrected data (red) and selected sub-set (black). Right: Corrected and selected data.

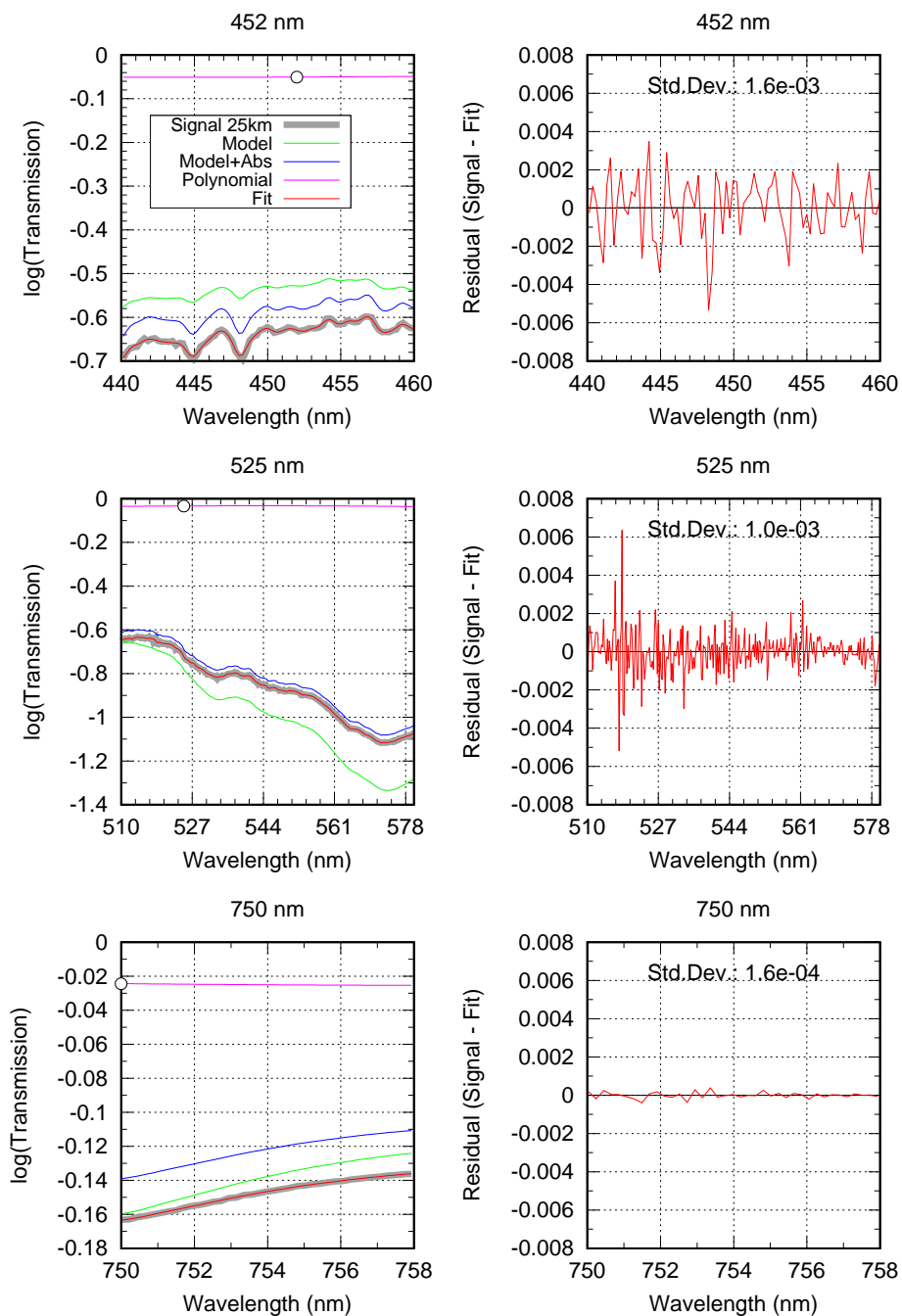


**Figure 6.** Example fit results for orbit 8014 (11 September 2003) and different wavelengths (left to right). Top: Spectrum at 25 km tangent height and related fit results. Bottom: Fit residual. The circle in the top plots marks the derived value for  $P_j(\lambda_{\text{ext}})$ .

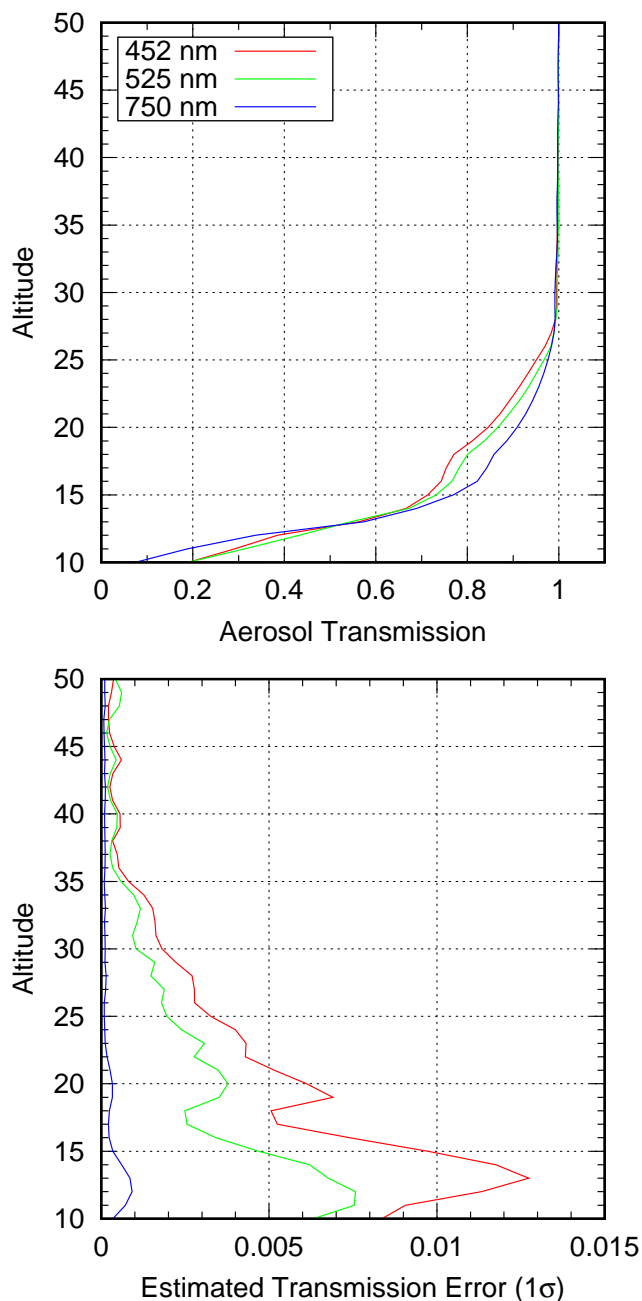


**Figure 7.** Aerosol transmissions (top) and corresponding errors (bottom) for orbit 8014 (11 September 2003) and different wavelengths.

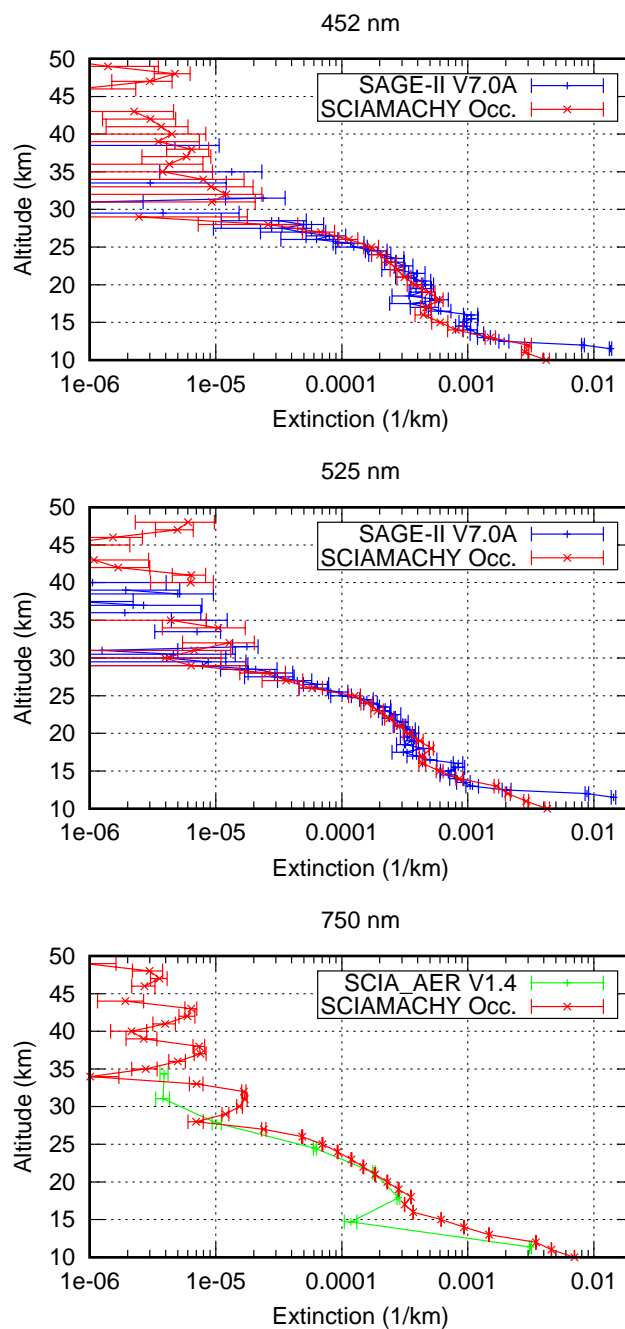


**Figure 8.** Retrieved extinction profiles from SCIAMACHY solar occultation (red), SAGE II product V7.00A (blue) and SCIAMACHY limb aerosol extinction product V1.4 (green) for orbit 8014 (11 September 2003) and different wavelengths (top to bottom).



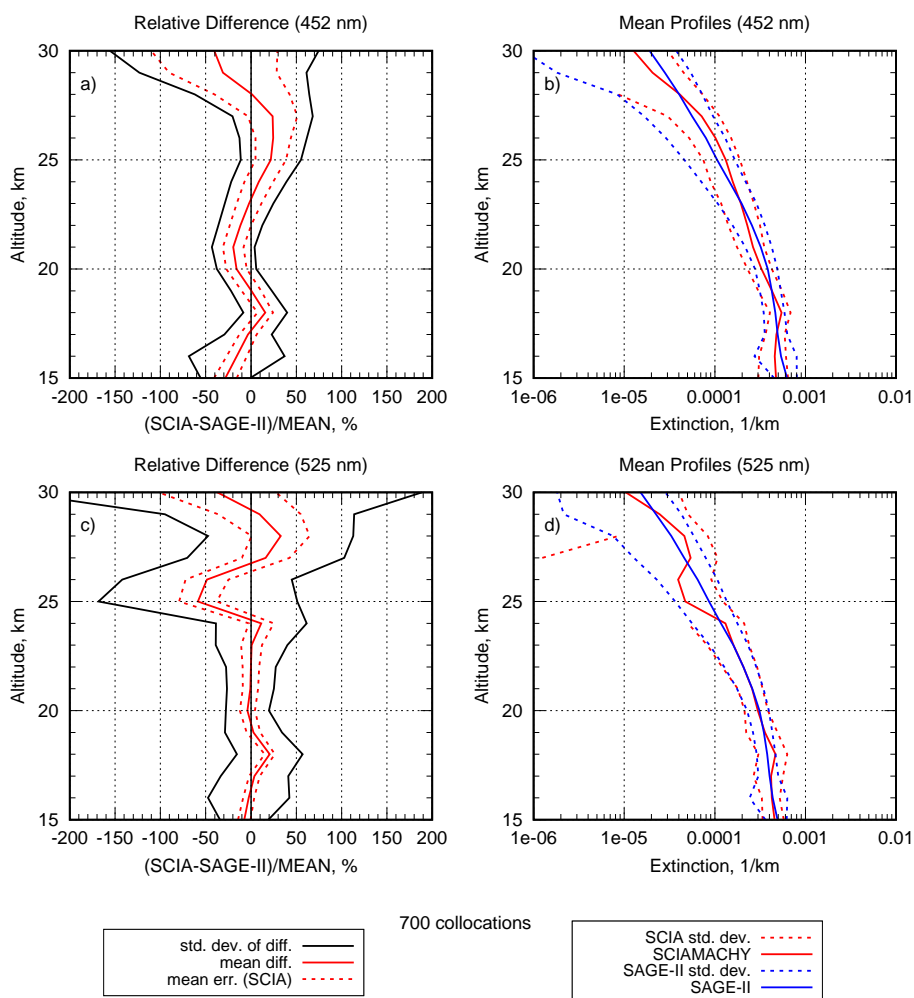


**Figure 9.** Comparison between extinction profiles from SCIAMACHY solar occultation and collocated SAGE II data. a) Relative differences at 452 nm (solid red), mean SCIAMACHY error (dashed red) and standard deviation of differences (black). b) Mean extinction profiles at 452 nm (solid) and corresponding standard deviations (dashed) for SCIAMACHY (red) and SAGE II (blue). c) same as a), but for 525 nm. d) same as b), but for 525 nm.

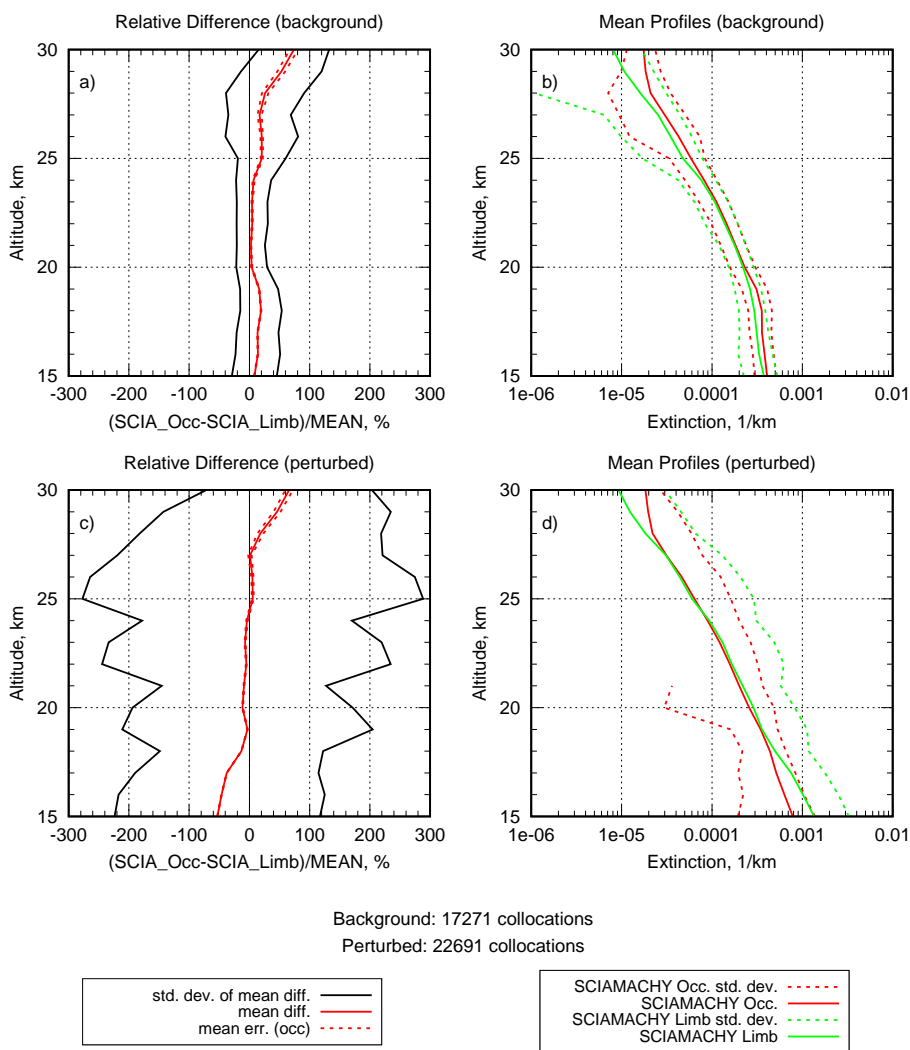


**Figure 10.** Similar as Fig. 9, but for 750 nm and comparison with SCIAMACHY limb aerosol extinctions. Top: Results for background times (i.e. extinctions always  $< 0.001$ ). Bottom: Results for perturbed times (all other data).

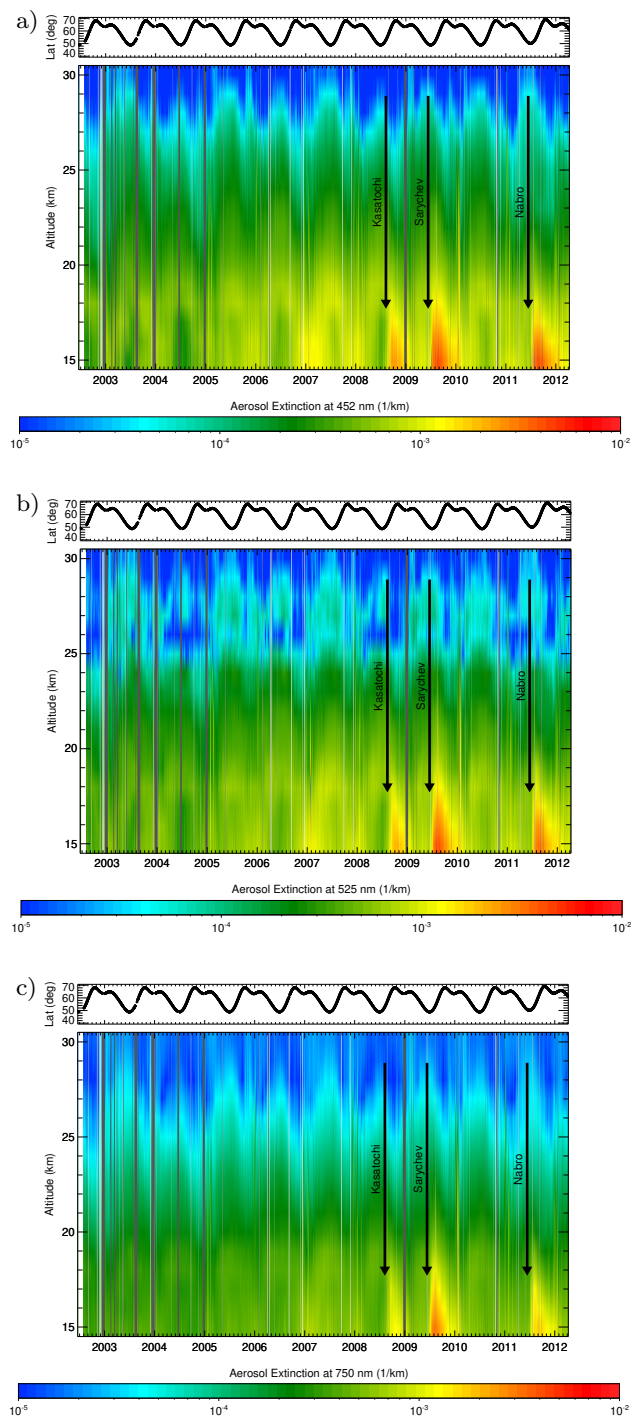


**Figure 11.** Time series of daily gridded aerosol extinction profiles from SCIAMACHY solar occultation at (from top to bottom) 452 nm, 525 nm and 750 nm. The start times of some major volcanic eruptions occurring at higher latitudes are marked. The top sub-plots show the mean latitude of the observations.

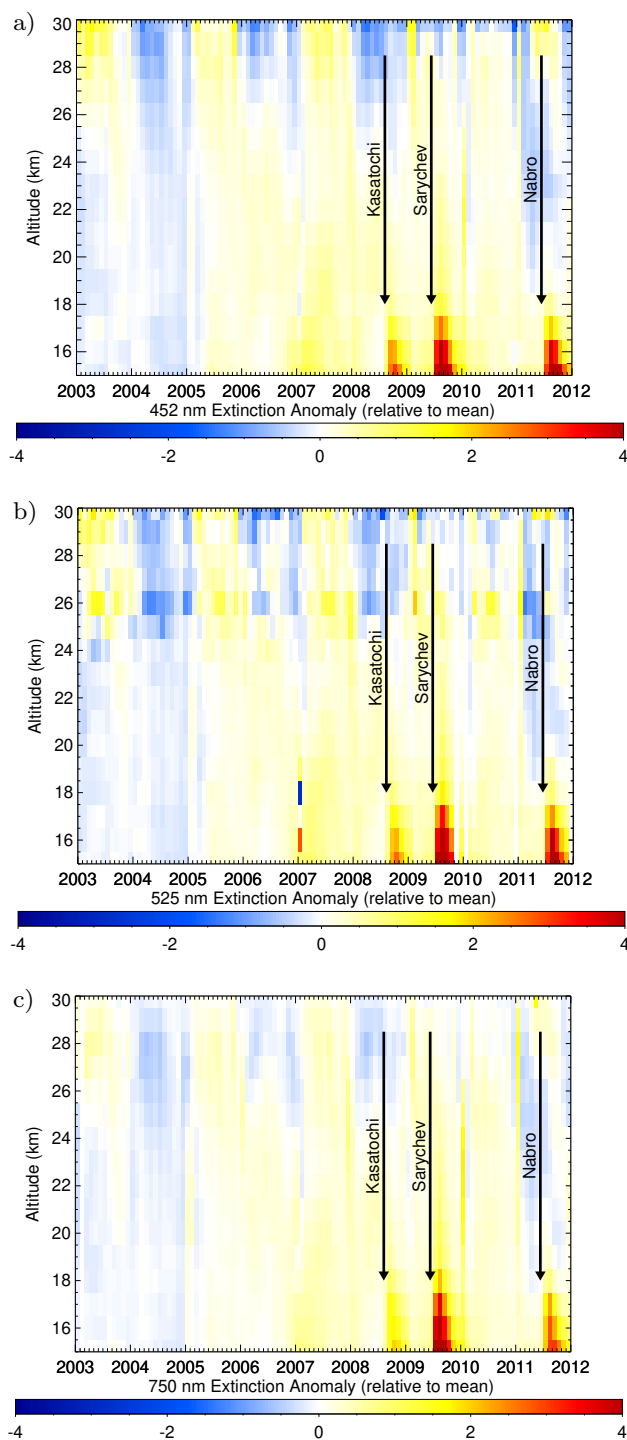


**Figure 12.** Time series of relative extinction anomalies from SCIAMACHY solar occultation at (from top to bottom) 452 nm, 525 nm and 750 nm. The start times of some major volcanic eruptions occurring at higher latitudes are marked.

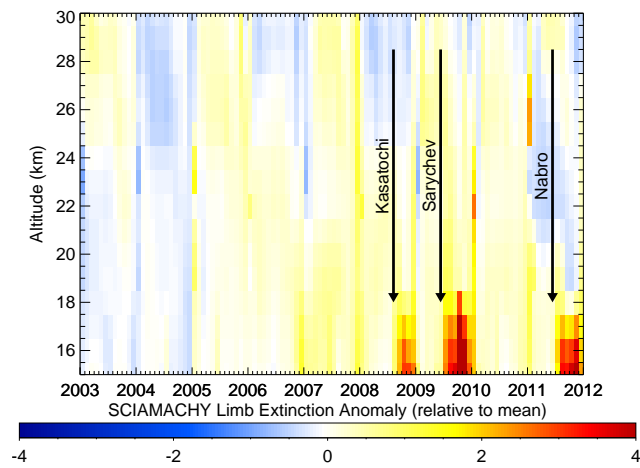


**Figure 13.** As Fig. 12, but for SCIAMACHY limb data at 750 nm.

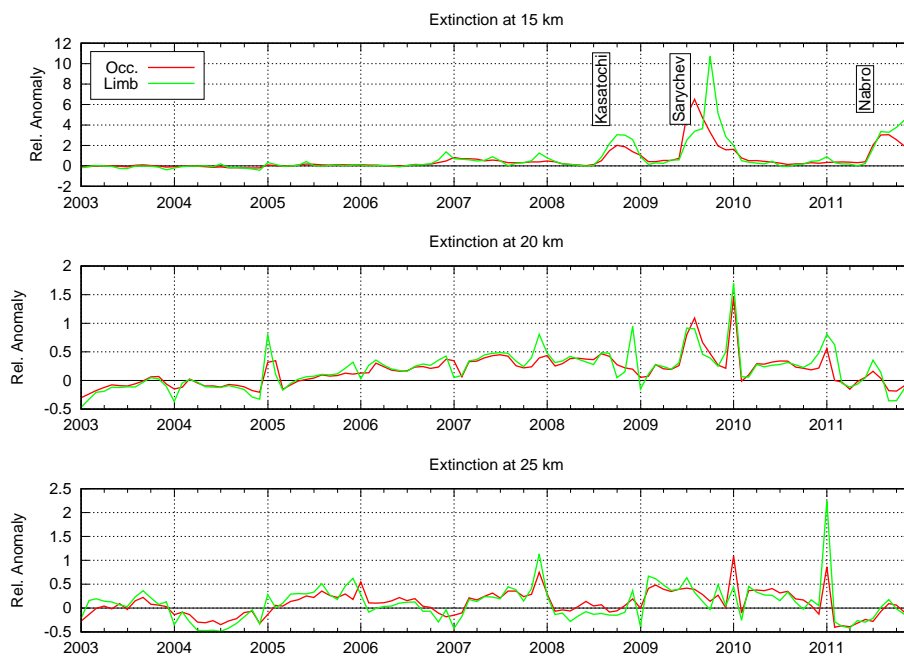


**Figure 14.** Time series of relative extinction anomalies at 750 nm for altitudes 15 km, 20 km and 25 km (top to bottom). Red: SCIAMACHY solar occultation data. Green: SCIAMACHY limb data.

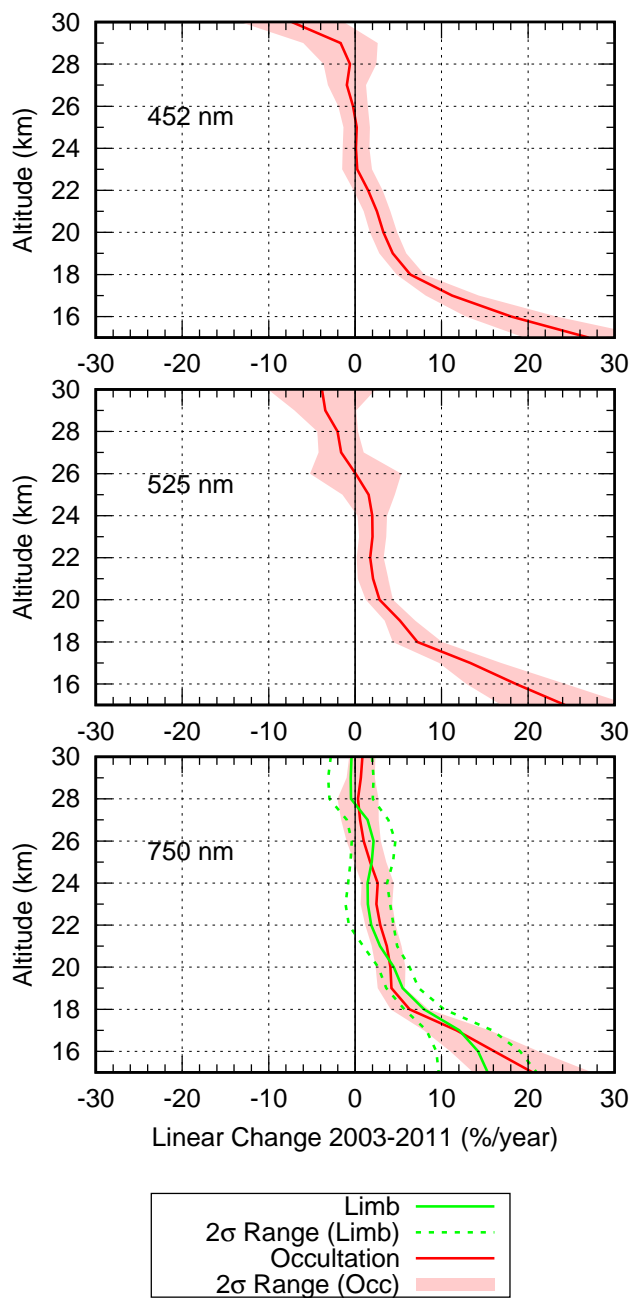


**Figure 15.** Linear changes of SCIAMACHY solar occultation (red) and SCIAMACHY limb extinctions (green) as function of altitude for the time interval 2003 to 2011. Values are given relative to the mean extinction 2003–2006. Top to bottom: Results for 452 nm, 525 nm and 750 nm. Shaded red areas and dashed green lines denote the  $2\sigma$  error range of the changes.



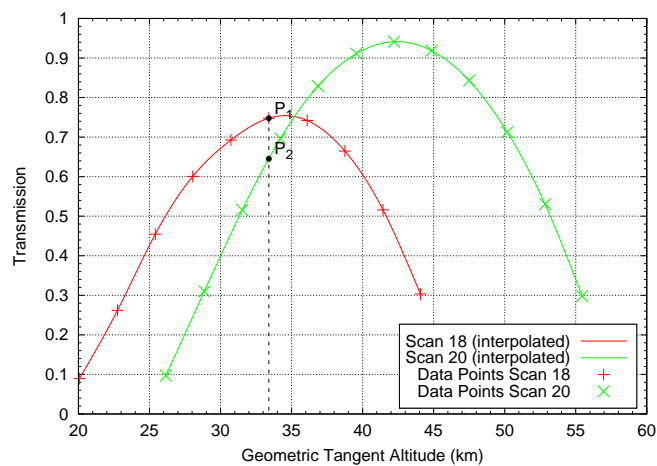


**Figure A1.** Bending angle fit. See text for explanation.

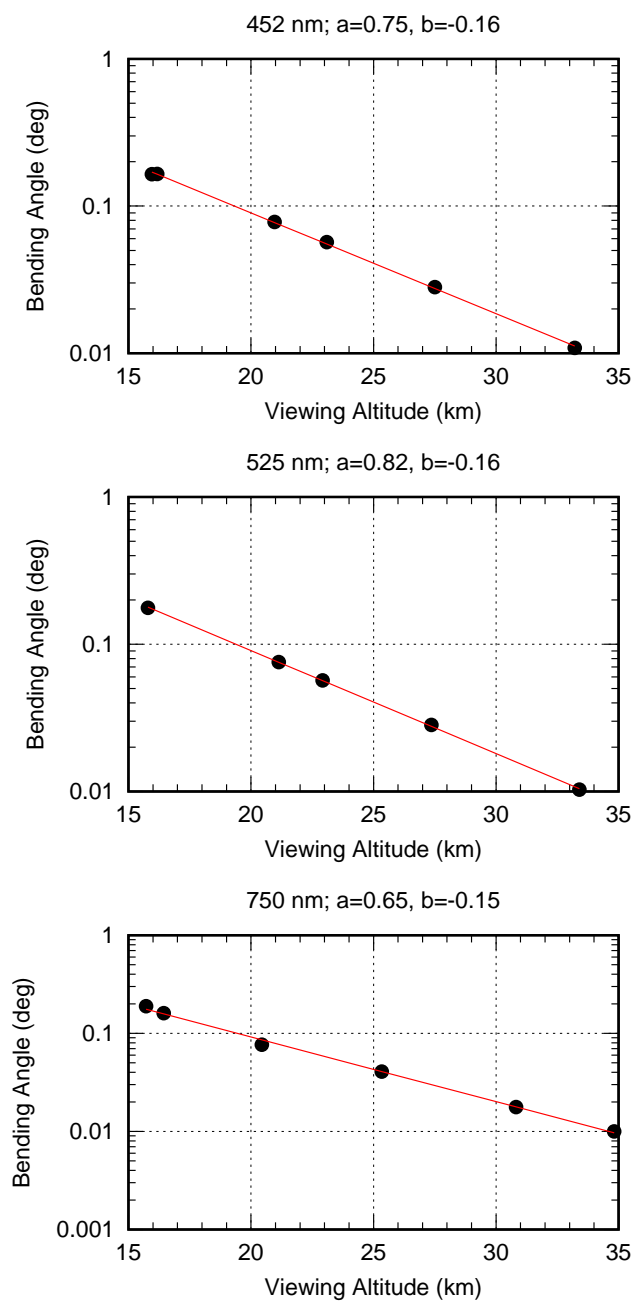


**Figure A2.** Fit of bending angle parameters  $a$  and  $b$  for different wavelengths.